that anomalous diffusion can displace the sulphuric acid spikes that are used as stratigraphic markers to correlate timescales between different ice cores and the tephra deposits contained in other sedimentary records[24]. Our model explains how diffusion preserves the amplitudes of anomalies in the c_B record, but the anomalies themselves are translated relative to the surrounding ice. Efforts should be made to account for this behaviour when analysing data from the older portions of ice cores by increasing spatial resolution. This could be particularly important when the relative timing of concentration peaks is needed to test theories for the causal links between the various climate proxies. □

Received 2 October 2000; accepted 2 April 2001.

1. Dansgaard, W. *et al.* Evidence for general instability of past climate from a 250-kyr ice-core record. *Nature* **364,** 218–220 (1993).
2. Petit, J. R. *et al.* Climate and atmospheric history of the past 420,000 years from the Vostok ice core, Antarctica. *Nature* **399,** 429–436 (1999).
3. Alley, R. B. Ice-core evidence of abrupt climate changes. *Proc. Natl Acad. Sci. USA* **97,** 1331–1334 (2000).
4. Dash, J. G., Fu, H. Y. & Wettlaufer, J. S. The premelting of ice and its environmental consequences. *Rep. Prog. Phys.* **58,** 115–167 (1995).
5. Wettlaufer, J. S. Ice surfaces: Macroscopic effects of microscopic structure. *Phil. Trans. R. Soc. Lond. A* **357,** 3403–3425 (1999).
6. Paterson, W. S. B. *The Physics of Glaciers* 3rd edn, 8–25 (Pergamon, Oxford, 1994).
7. Wolff, E. W. in *Chemical Exchange Between the Atmosphere and Polar Ice* (eds Wolff, E. W. & Bales, R. C.) 541–560 (NATO ASI Series I, Vol. 43, Springer, Berlin, 1996).
8. Ramseier, R. O. Self-diffusion of tritium in natural and synthetic ice monocrystals. *J. Appl. Phys.* **38,** 2553–2556 (1967).
9. Nye, J. F. in *Physics and Chemistry of Ice* (eds Maeno, N. & Hondoh, T.) 200–205 (Hokkaido Univ. Press, 1992).
10. Nye, J. F. The geometry of water veins and nodes in polycrystalline ice. *J. Glac.* **35,** 17–22 (1989).
11. Mader, H. M. Observations of the water-vein system in polycrystalline ice. *J. Glac.* **38,** 333–347 (1992).
12. Nye, J. F. Diffusion of isotopes in the annual layers of ice sheets. *J. Glac.* **44,** 467–468 (1998).
13. Johnsen, S. J. *et al.* in *Ice Physics and the Natural Environment* (eds Wettlaufer, J. S., Dash, J. G. & Untersteiner, N.) 89–107 (NATO ASI Series I, Vol. 56, Springer, Berlin, 1999).
14. Gundestrup, N. S., Dahl-Jensen, D., Johnsen, S. J. & Rossi, A. Bore-hole survey at dome GRIP—1991. *Cold Reg. Sci. Technol.* **21,** 399–402 (1993).
15. Cuffey, K. M. *et al.* Large Arctic temperature-change at the Wisconsin–Holocene glacial transition. *Science* **270,** 455–458 (1995).
16. Weast, R. C. (ed.) *CRC Handbook of Chemistry and Physics* 68th edn, D219–D269 (CRC Press, Boca Raton, 1987).
17. Mulvaney, R., Wolff, E. W. & Oates, K. Sulphuric acid at grain-boundaries in Antarctic ice. *Nature* **331,** 247–249 (1988).
18. Fukazawa, H., Sugiyama, K., Mae, S. J., Narita, H. & Hondoh, T. Acid ions at triple junction of Antarctic ice observed by Raman scattering. *Geophys. Res. Lett.* **25,** 2845–2848 (1998).
19. Wood, S. E. & Battino, R. *Thermodynamics of Chemical Systems* (Cambridge Univ. Press, Cambridge, 1990).
20. Gross, G. W., Chen-ho, W., Bryant, L. & McKee, C. Concentration dependent solute redistribution at the ice/water phase boundary. II. Experimental investigation. *J. Chem. Phys.* **62,** 3085–3092 (1975).
21. Thorsteinsson, T., Kipfstuhl, J., Eicken, H., Johnsen, S. J. & Fuhrer, K. Crystal size variations in Eemian-age ice from the GRIP ice core, central Greenland. *Earth Planet. Sci. Lett.* **131,** 381–394 (1995).
22. Steffensen, J. P., Clausen, H. B., Hammer, C. U., Legrand, M. & De Angelis, M. The chemical composition of cold events within the Eemian section of the Greenland Ice Core Project ice core from Summit. *J. Geophys. Res.* **102,** 26747–26754 (1997).
23. Alley, R. B. *et al.* Comparison of deep ice cores. *Nature* **373,** 393–394 (1995).
24. Zielinski, G. A. Use of paleo-records in determining variability within the volcanism-climate system. *Quat. Sci. Rev.* **19,** 417–438 (2000).
25. Smith, C. S. Grains, phases and interfaces: An introduction to microstructure. *Trans. Metall. Soc. AIME* **175,** 15–51 (1948).
26. Ohtomo, M. & Wakahama, G. Growth-rate of recrystallization in ice. *J. Phys. Chem.* **87,** 4139–4142 (1983).
27. Dansgaard, W. & Johnsen, S. J. A flow model and a time scale for the ice core from Camp Century, Greenland. *J. Glac.* **8,** 215–223 (1969).
28. Cuffey, K. M. & Clow, G. D. Temperature, accumulation, and ice sheet elevation in central Greenland through the last deglacial transition. *J. Geophys. Res.* **102,** 26383–26396 (1997).
29. Thorsteinsson, T., Kipfstuhl, J. & Miller, H. Textures and fabrics in the GRIP ice core. *J. Geophys. Res.* **102,** 26583–26599 (1997).
30. De la Chapelle, S., Castelnau, O., Lipenkov, V. & Duval, P. Dynamic recrystallization and texture development in ice as revealed by the study of deep ice cores in Antarctica and Greenland. *J. Geophys. Res.* **103,** 5091–5105 (1998).

Supplementary information is available from *Nature*'s World-Wide Web site (http://www.nature.com) or as paper copy from the London editorial office of *Nature*.

Acknowledgements

We acknowledge R. Alley, J. G. Dash, D. P. Winebrenner, S. G. Warren, G. W. Gross, S. F. Johnsen, J. F. Nye, E. J. Steig, J. P. Steffensen and E. W. Wolff for discussions that have influenced this work. We also thank H. M. Mader for providing the photograph for Figure 1b. Support for this research has been provided by the US National Science Foundation.

Correspondence and requests for materials should be addressed to A.W.R. (e-mail: awrempel@apl.washington.edu).

The post-spinel transformation in Mg_2SiO_4 and its relation to the 660-km seismic discontinuity

Sang-Heon Shim*, Thomas S. Duffy* & Guoyin Shen†

** Department of Geosciences, Princeton University, Princeton, New Jersey 08544, USA*

† CARS, University of Chicago, Chicago, Illinois 60637, USA

The 660-km seismic discontinuity in the Earth's mantle has long been identified with the transformation of $(Mg,Fe)_2SiO_4$ from γ-spinel (ringwoodite) to $(Mg,Fe)SiO_3$-perovskite and (Mg,Fe)O-magnesiowüstite. This has been based on experimental studies of materials quenched from high pressure and temperature[1–3], which have shown that the transformation is consistent with the seismically observed sharpness and the depth of the discontinuity at expected mantle temperatures[4]. But the first *in situ* examination of this phase transformation in Mg_2SiO_4 using a multi-anvil press[5] indicated that the transformation occurs at a pressure about 2 GPa lower than previously thought (equivalent to ~600 km depth) and hence that it may not be associated with the 660-km discontinuity. Here we report the results of an *in situ* study of Mg_2SiO_4 at pressures of 20–36 GPa using a combination of double-sided laser-heating and synchrotron X-ray diffraction in a diamond-anvil cell. The phase transformation from γ-Mg_2SiO_4 to $MgSiO_3$-perovskite and MgO (periclase) is readily observed in both the forward and reverse directions. In contrast to the *in situ* multi-

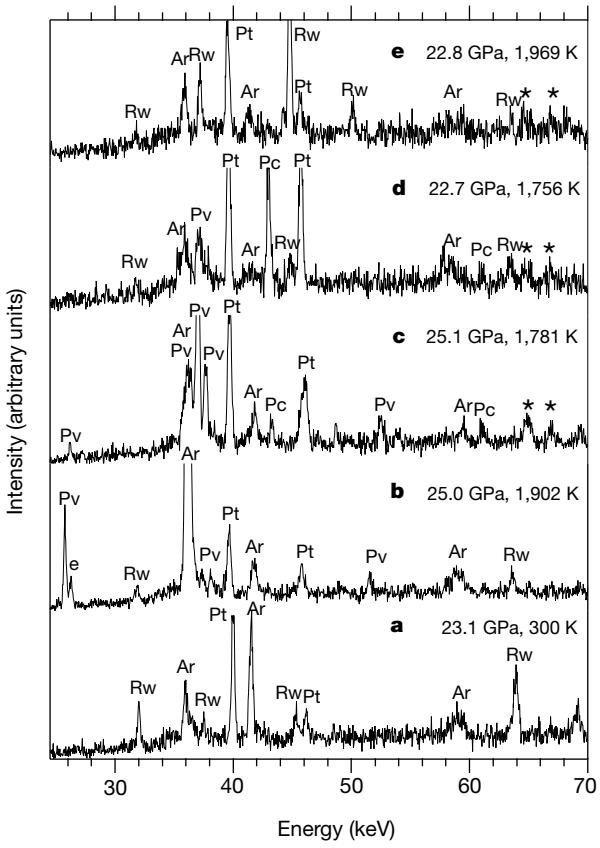

Figure 1 a–e, Representative X-ray diffraction patterns at the indicated *P–T* conditions. Peak identifications are: Rw, ringwoodite; Pv, perovskite; Pc, periclase; Pt, platinum; Ar, argon; asterisk, platinum fluorescence; e, detector escape peak.

anvil-press study[5], we find that the pressure and temperature of the post-spinel transformation in Mg_2SiO_4 is consistent with seismic observations[4,6] for the 660-km discontinuity.

Pure synthetic forsterite was mixed with 10 wt% platinum which serves as an internal pressure scale and laser absorber. A 15-μm-thick foil of the sample mixture was loaded in a 100-μm hole in a steel gasket and compressed by 300-μm diamond anvils. Argon served as a pressure transmitting and insulation medium. Ruby chips were also loaded in an unheated area.

The laser-heating system at the GSECARS sector of the Advanced Photon Source provides a radially homogeneous temperature profile over 20–30 μm by using a TEM_{01} Nd:YLF laser mode, and reduces the axial thermal gradient by heating from both sides[7,8]. Temperature profiles were measured using imaging spectrometers on each side. Temperature was determined by fitting the radiation spectra, corrected for system response, to Planck's equation. A three-dimensional averaging technique was used to calculate the mean temperature over the volume exposed to X-rays[7]. Including radial and axial gradients, temperature fluctuations during X-ray exposure, and the fitting residual, the temperature uncertainty (1σ) was ± 50–150 K in these experiments.

Energy dispersive X-ray diffraction measurements were performed using a small (5 μm × 7 μm) horizontally focused X-ray beam and a solid-state detector (Fig. 1). We oscillated the diamond cell (±20°) about its loading axis to minimize the effect of preferred orientation. The primary pressure scale used here is the pressure–volume–temperature (P–V–T) equation of state (EOS) of platinum[9]. Pressure was also measured using the ruby scale[10] before and after heating.

Below 20 GPa, we performed two heating runs to synthesize ringwoodite. The pressure was then increased to 20.4 GPa and a third run was performed. We observed an increase of 2–4 GPa during heating due to the thermal pressure[11,12]. After 20 minutes of heating, the periclase (200) peak appeared and co-existed with ringwoodite diffraction lines. By increasing the temperature from 1,672(50) K to 1942(75) K (numbers in parentheses are 1σ uncertainties), we observed a pressure decrease from 24.6(4) GPa to 22.3(6) GPa as a result of thermal relaxation[13] (see P–T path for run 3 in Fig. 2). At this point, the periclase (200) line disappeared, owing to back transformation to the lower-pressure phase. In the fourth run, we increased pressure to 23.1 GPa (Fig. 1a). After eight minutes of heating, diagnostic perovskite lines, (002)+(110) and (004)+(220) doublets, appeared (Fig. 1b). The periclase (200) line was also observed in other patterns during this run. We performed two more runs at 25–29 GPa (run 5 in Fig. 2) and 30–35 GPa, where we observed complete transformation from ringwoodite to perovskite+periclase (Fig. 1c). To observe the transformation from perovskite+periclase to ringwoodite, we decreased pressure and performed three heating runs at 27–30, 25–26 and 21–25 GPa. For the last run, ringwoodite appeared after 6 minutes of heating and the transformation was complete after 24 minutes (Fig. 1d, e). Additional details regarding the P–T paths are provided in the Supplementary Information.

We observe that the low- and high-pressure phase assemblages coexist within a range of about 2 GPa (Fig. 2). This scatter is due to both temperature uncertainty and kinetic effects. The temperature uncertainty is 50–150 K, and this propagates to a pressure uncertainty of 0.3–0.9 GPa. Kinetics and the P–T path may also be important. For example, as shown above in the P–T path for run 3 (Fig. 2), we observed that the high-pressure assemblage synthesized above the phase boundary can survive at slightly below the phase boundary for 5 minutes before complete back transformation.

Using data points for which we observed a mixture of low- and high-pressure phases, we obtained the phase boundary. We fixed the slope of the phase boundary to the average from two multi-anvil studies[2,5] (−2.75 MPa K^{-1}), because our data scatter precludes constraining the slope reliably. A weight was assigned to each data point using its pressure and temperature uncertainties. The transformation pressure was found to be 23.7 ± 1.1 GPa at 1,800 K. However, the boundary obtained in ref. 5 is 2.6 GPa lower than this, which is a statistically significant difference at the 2σ level (Fig. 2).

In order to examine this result, we investigated several error sources. In the laser-heated diamond cell, the greatest error source is the temperature uncertainty[14]. The error in temperature propagates to pressure through the thermal-pressure term. The sensitivity of pressure for temperature, $(\partial P/\partial T)_P$, is calculated for platinum using its P–V–T EOS[9]. To have a 2.6-GPa error, the temperature must be overestimated by 380 K. However, including all random error sources, our temperature uncertainty is less than 150 K. Systematic error sources have also been examined, and are estimated to be less than 100 K for this heating system[8]. Using lattice strain theory[15],

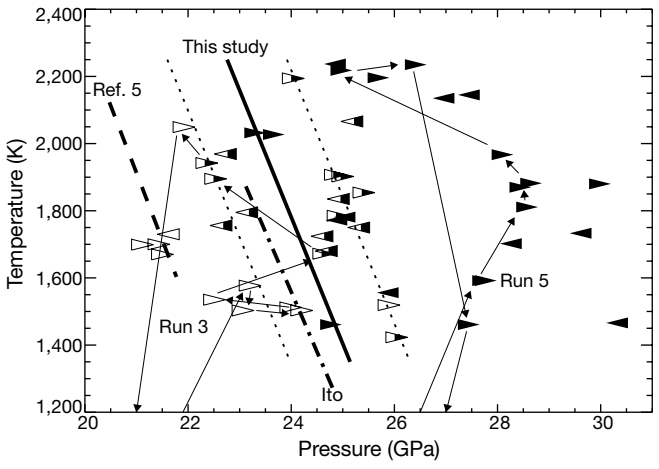

Figure 2 Phase diagram of Mg_2SiO_4. Right-pointing and left-pointing triangles represent respectively data points obtained during compression and decompression. The presence of ringwoodite is shown by open symbols and that of perovskite+periclase is shown by solid symbols. Half-filled symbols represent coexistence of ringwoodite and perovskite+periclase. Two representative P–T paths during heating runs (run 3 and 5) are shown by thin solid lines with arrowheads. The heavy dash-dotted and dashed lines show phase boundaries from previous studies[2,5]. The phase boundary obtained here is shown by the heavy solid line with 1σ uncertainty (thin dotted lines).

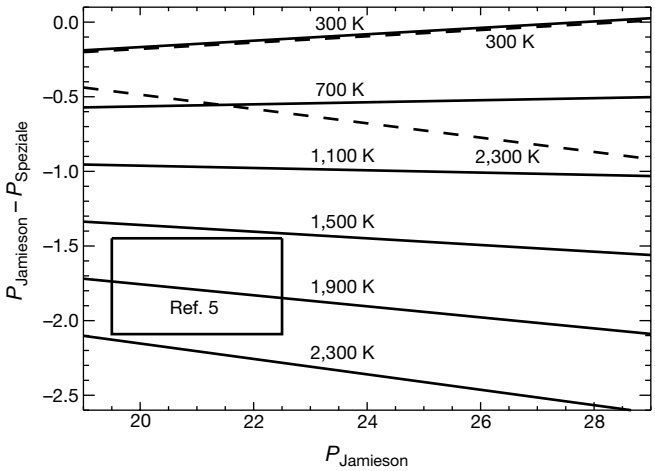

Figure 3 Pressure difference between two equations of state for periclase[16,20] at different P–T conditions. The P–T range in the experiments of ref. 5 is indicated by the rectangle. The effect of changing the Grüneisen parameter in the EOS of Speziale *et al.*[16] to the value used by Jamieson *et al.*[20] is shown by dashed lines. See text for details. $P_{Jamieson}$ and $P_{Speziale}$ are the pressures calculated using the MgO EOS from refs 20 and 16, respectively.

differential stresses were also investigated and found to be negligible at high temperature.

We also compared pressures obtained from different materials in our sample, such as periclase[16] and ringwoodite[17]. On average, the platinum pressure scale[9] overestimates pressure by 0.2 GPa compared to periclase and by 2.0 GPa compared to ringwoodite. We also examined the difference between platinum and ruby pressures before and after heating. On average, platinum yields a larger pressure by ~1.2 GPa. However, the ruby chips were located at the edge of the sample chamber where the pressure should be lower, owing to the radial gradient. Thus, except for ringwoodite, all pressures are internally consistent within 1.2 GPa.

One possibility for the discrepancy between our result and those of Irifune *et al.*[5] is the inconsistency of the equations of state of platinum and gold. Irifune *et al.* justified the use of the gold pressure scale of ref. 18 on the basis of an earlier study[19] that found good agreement between the gold EOS of Anderson *et al.*[18] and the periclase EOS by Jamieson *et al.*[20] In our study, we observed that the platinum pressure scale by Holmes *et al.*[9] shows good agreement with the periclase pressure scale by Speziale *et al.*[16]. Thus by comparing the periclase EOS values, we can obtain an intercomparison of gold and platinum. Figure 3 shows the difference between the periclase EOS of Jamieson *et al.*[20] and Speziale *et al.*[16] We observe a maximum difference of 2.1 GPa between the two periclase pressure calculations at P–T conditions of the post-spinel transformation. This means that the gold EOS[18] yields ~2 GPa lower pressure than the platinum EOS[9]. We also observed a 2 GPa underestimation of pressure by the ringwoodite EOS[17], which was also obtained using the gold pressure scale of ref. 18.

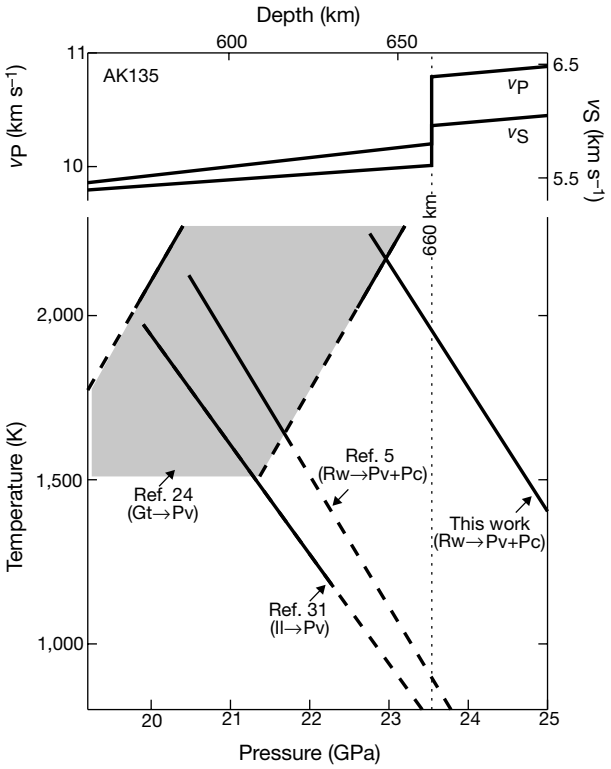

Figure 4 Seismic velocity profiles[6] and phase boundaries of mantle constituents near the 660-km discontinuity. Top, P-wave and S-wave velocities as a function of depth in the Earth. Data from earth model AK135 (ref. 6). Bottom, phase boundaries of mantle constituents (solid lines, dashed where extrapolated). The post-ilmenite (Il⟶Pv, where Il indicates ilmenite and Pv indicates perovskite) boundary is from ref. 31. The post-garnet (Gt⟶Pv) transformation with 6 mol% Al_2O_3 (from ref. 24) is plotted as a shaded area where majorite garnet (Gt) and perovskite coexist. The post-spinel (Rw⟶Pv+Pc, where Rw indicates ringwoodite and Pc indicates periclase) boundaries are from ref. 5 and this study.

The discrepancy between the two periclase scales is mainly caused by the use of different Grüneisen parameters. As shown in Fig. 3, the discrepancy decreases drastically just by changing the Grüneisen parameter used by Speziale *et al.*[16] (1.52 ± 0.05) to the value used by Jamieson *et al.*[20] (1.32). The former workers obtained the Grüneisen parameter using a thermodynamic relationship, $\gamma = \alpha K_S/\rho C_P$ (α is the thermal expansivity, K_S is the adiabatic bulk modulus, ρ is the density and C_P is the isobaric heat capacity), and accurately determined thermodynamic parameters, whereas the value used by the latter workers was based on low-accuracy estimates from porous shock wave data. In addition, the EOS of Speziale *et al.*[16] satisfies a wide range of high P–T data including static compression[21,22] and shock wave data[23].

A recent study[24] that intercompared pressure standards suggested that the gold and platinum pressure scales are consistent. However, this study also found that various different standards yield pressures that differ by ~2 GPa at 24 GPa. We also note that Anderson later concluded that the gold EOS may not be reliable[25]. These results emphasize the need for further studies of pressure standards. Other possible sources of systematic error—such as the effect of pressure on thermocouple e.m.f. in multi-anvil studies[26], temperature gradients, deviatoric stress, and stress inhomogeneity—also need to be investigated.

Phase boundaries for mantle minerals determined using *in situ* techniques at pressures near 660-km depth are shown in Fig. 4. Apart from this work, all determinations were performed in the multi-anvil press using the gold scale of Anderson *et al.*[18]. The post-spinel and post-ilmenite boundaries yield low temperatures (< 900 K) at 660-km depth. However, a variety of geophysical constraints including xenoliths, basalt melting temperatures, and *in situ* data for the α–β transformation in Mg_2SiO_4 suggest that transition zone temperatures are ~1,600–1,900 K (refs 27–29). At these temperatures, the post-spinel boundary would occur at ~610-km depth. Because no discontinuity is observed near here, this would place severe limits on the olivine abundance of the transition zone and further require that the 660-km discontinuity be associated with a chemical change or the garnet–perovskite transformation. However, seismological data suggest the 660-km discontinuity does not prevent the penetration of subducting stabs[30]. Furthermore, to associate the post-garnet boundary[24] with the 660-km discontinuity, aluminium enrichment relative to pyrolite is required. Although the thickness and depth of this boundary will be affected by bulk composition[24], the slope of post-garnet boundary conflicts with the seismically observed negative Clapeyron slope of the 660-km discontinuity[4]. In contrast, our observations of the post-spinel transformation are fully consistent with geophysical data for the 660-km discontinuity.

We have thus shown that the laser-heated diamond-anvil cell can accurately determine phase boundaries of mantle constituents. We find that the post-spinel phase boundary lies within a plausible mantle temperature range at 660 km depth, and thus this transformation remains the best candidate to explain this seismic discontinuity. □

Received 25 October 2000; accepted 6 April 2001.

1. Liu, L.-G. Post-oxide phases of forsterite and enstatite. *Geophys. Res. Lett.* **2,** 417–419 (1975).
2. Ito, E. & Takahashi, E. Postspinel transformations in the system Mg_2SiO_4–Fe_2SiO_4 and some geophysical implications. *J. Geophys. Res.* **94,** 10637–10646 (1989).
3. Ito, E., Akaogi, M., Topor, L. & Navrotsky, A. Negative pressure-temperature slopes for reactions forming $MgSiO_3$ perovskite from calorimetry. *Science* **249,** 1275–1278 (1990).
4. Helffrich, G. Topography of the transition zone seismic discontinuities. *Rev. Geophys.* **38,** 141–158 (2000).
5. Irifune, T. *et al.* The postspinel phase boundary in Mg_2SiO_4 determined by in situ X-ray diffraction. *Science* **279,** 1698–1700 (1998).
6. Kennett, B. L. N., Engdahl, E. R. & Buland, R. Constraints on seismic velocities in the Earth from travel times. *Geophys. J. Int.* **122,** 108–124 (1995).
7. Shim, S.-H., Duffy, T. S. & Shen, G. The stability and P–V–T equation of state for $CaSiO_3$ perovskite in the earth's lower mantle. *J. Geophys. Res.* **105,** 25955–25968 (2000).
8. Shen, G., Rivers, M. L., Wang, Y. & Sutton, S. R. Laser heated diamond cell system at the Advanced Photon Source for in situ x-ray measurements at high pressure and temperature. *Rev. Sci. Instrum.* **72,** 1273–1282 (2001).

9. Holmes, N. C., Moriarty, J. A., Gathers, G. R. & Nellis, W. J. The equation of state of platinum to 660 GPa (6.6 Mbar). *J. Appl. Phys.* **66,** 2962–2967 (1989).
10. Mao, H.-K., Xu, J. & Bell, P. M. Calibration of the ruby pressure gauge to 800 kbar under quasihydrostatic conditions. *J. Geophys. Res.* **91,** 4673–4676 (1986).
11. Heinz, D. L. Thermal pressure in the laser-heated diamond anvil cell. *Geophys. Res. Lett.* **17,** 1161–1164 (1990).
12. Fiquet, G. *et al.* X-ray diffraction of periclase in a laser-heated diamond-anvil cell. *Phys. Earth Planet. Inter.* **95,** 1–17 (1996).
13. Kavner, A. & Duffy, T. S. Pressure-volume-temperature paths in the laser-heated diamond anvil cell. *J. Appl. Phys.* **89,** 1907–1914 (2001).
14. Boehler, R. High-pressure experiments and the phase diagram of lower mantle and core materials. *Rev. Geophys.* **38,** 221–245 (2000).
15. Singh, A. K. The lattice strains in a specimen (cubic system) compressed nonhydrostatically in an opposed anvil device. *J. Appl. Phys.* **73,** 4278–4286 (1993).
16. Speziale, S. *et al.* Quasi-hydrostatic compression of magnesium oxide to 52 GPa: implications for the pressure–volume–temperature equations of state. *J. Geophys. Res.* **106,** 515–528 (2001).
17. Meng, Y. *et al.* In situ high P–T X-ray diffraction studies on three polymorphs (α, β, γ) of Mg_2SiO_4. *J. Geophys. Res.* **98,** 22199–22207 (1993).
18. Anderson, O. L., Isaak, D. G. & Yamamoto, S. Anharmonicity and the equation of state for gold. *J. Appl. Phys.* **65,** 1534–1543 (1989).
19. Funamori, N. *et al.* Thermoelastic properties of $MgSiO_3$ perovskite determined by in situ X-ray observations up to 30 GPa and 2000 K. *J. Geophys. Res.* **101,** 8257–8269 (1996).
20. Jamieson, J. C., Frits, J. N. & Manghnani, M. H. in *High-Pressure Research in Geophysics* (eds Akimoto, S. & Manghnani, M. H.) 27–48 (Center for Academic Publications, Tokyo, 1982).
21. Fei, Y. Effect of temperature and composition on the bulk modulus of (Mg,Fe)O. *Am. Mineral.* **84,** 272–276 (1999).
22. Dewaele, A., Fiquet, G., Andrault, D. & Häusermann, D. P–V–T equation of state of periclase from synchrotron radiation measurements. *J. Geophys. Res.* **105,** 2869–2877 (2000).
23. Svendsen, B. & Ahrens, T. J. Shock-induced temperatures of MgO. *Geophys. J. R. Astron. Soc.* **91,** 667–691 (1987).
24. Hirose, K. *et al.* In situ measurements of the phase transition boundary in $Mg_3Al_2Si_3O_{12}$: implications for the nature of the seismic discontinuities in the Earth's mantle. *Earth Planet. Sci. Lett.* **184,** 567–573 (2001).
25. Anderson, O. L. The volume dependence of thermal pressure in perovskite and other minerals. *Phys. Earth Planet. Inter.* **112,** 267–283 (1999).
26. Rubie, D. C. Characterising the sample environment in multianvil high-pressure experiments. *Phase Transit.* **68,** 431–451 (1999).
27. Jackson, I. & Ridgen, S. M. in *The Earth's Mantle: Composition, Structure, and Evolution* (ed. Jackson, I.) 405–460 (Cambridge University Press, New York, 1998).
28. Vacher, P., Mocquet, A. & Sotin, C. Computation of seismic profiles from mineral physics: the importance of the non-olivine components for explaining the 660 km depth discontinuity. *Phys. Earth Planet. Inter.* **106,** 275–298 (1998).
29. Morishima, H. *et al.* The phase boundary between α-Mg_2SiO_4 and β-Mg_2SiO_4 determined by in-situ X-ray observation. *Science* **265,** 1202–1203 (1994).
30. van der Hilst, R. D., Widiyantoro, S. & Engdahl, E. R. Evidence for deep mantle circulation from global tomography. *Nature* **386,** 578–584 (1997).
31. Kuroda, K. *et al.* Determination of the phase boundary between ilmenite and perovskite in $MgSiO_3$ by in situ X-ray diffraction and quench experiments. *Phys. Chem. Mineral.* **27,** 523–532 (2000).

Supplementary information is available on *Nature*'s World-Wide Web site (http://www.nature.com) or as paper copy from the London editorial office of *Nature*.

Acknowledgements

We thank S. Speziale for experimental assistance, and F. Dahlen, T. Irifune, Y. Fei, O. Anderson and I. Jackson for discussions. This work was supported by the NSF.

Correspondence and requests for materials should be addressed to S.-H.S. (e-mail: sangshim@princeton.edu).

High-pressure polymorphs of olivine and the 660-km seismic discontinuity

L. Chudinovskikh & R. Boehler

Max-Planck Institut für Chemie, Postfach 3060, 55020 Mainz, Germany

It had long been accepted that the 400-km seismic discontinuity in the Earth's mantle results from the phase transition of $(Mg,Fe)_2SiO_4$-olivine to its high-pressure polymorph β-spinel (wadsleyite), and that the 660-km discontinuity results from the breakdown of the higher-pressure polymorph γ-spinel (ringwoodite) to $MgSiO_3$-perovskite and (Mg,Fe)O-magnesiowüstite[1–4]. An *in situ* multi-anvil-press X-ray study[5] indicated, however, that the phase boundary of the latter transition occurs at pressures 2 GPa lower than had been found in earlier studies using multi-anvil

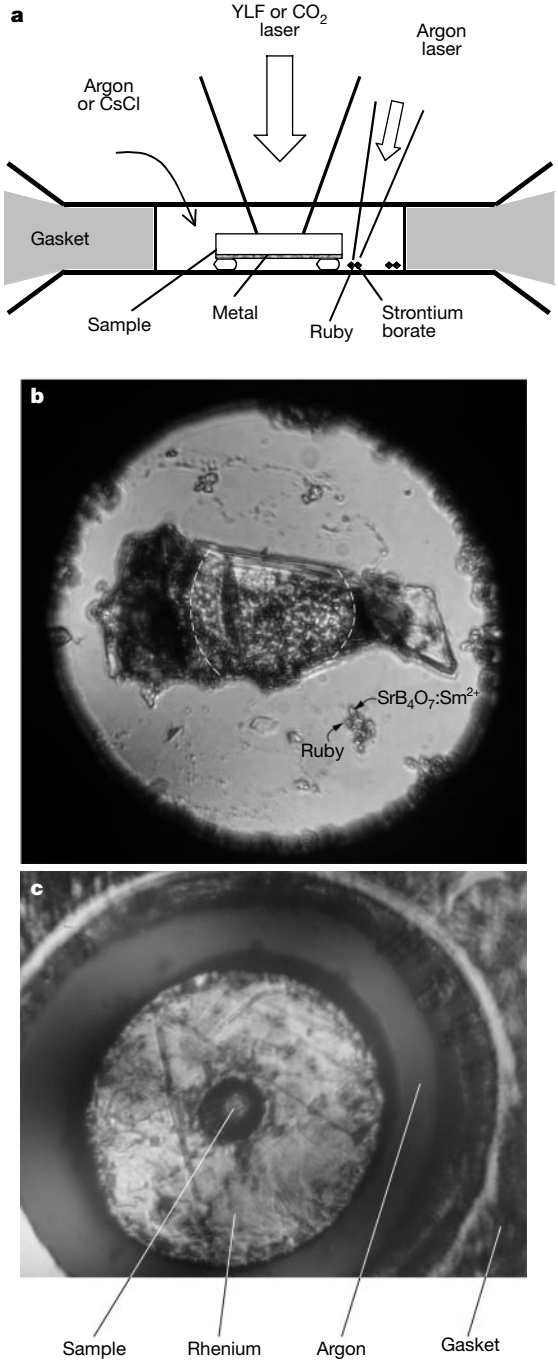

Figure 1 Diamond-cell arrangements used in this study to heat samples of Mg_2SiO_4-forsterite. **a**, Schematic cross-section. Samples were polished disks of pure, synthetic Mg_2SiO_4-forsterite, 10–15 μm thick and with diameters of 20 to 100 μm, thermally insulated from the bottom diamond by grains of forsterite. Argon or CsCl were used as pressure media. The pressure chambers were typically 170–180 μm in diameter and 45–55 μm in thickness. The samples were either heated directly with a 150 W CO_2 laser ($\lambda = 10.5$ μm), or were sputtered with films of Mo, Re or Cr (<1 μm thick) and then heated with a 50 W YLF (yttrium-lithium-fluoride) laser ($\lambda = 1.05$ μm)—and in some experiments with the combined beams of an additional 20 W YLF laser. **b**, Molybdenum-sputtered forsterite sample after heating. The heated portion showed full conversion to γ-Mg_2SiO_4. Thermal pressure increase was measured from two adjacent grains of ruby and strontium borate excited with an argon laser. **c**, Small crystal (15–20 μm in size) inside a Re microfurnace with outer diameter 80 μm, inner diameter 20 μm, and a thickness of 30 μm. This furnace was uniformly heated with the YLF laser in an argon pressure medium. This heating method essentially eliminated temperature gradients in the sample.